ELSEVIER

Contents lists available at ScienceDirect

Journal of Materials Science & Technology

journal homepage: www.elsevier.com/locate/jmst



Precipitation and coarsening kinetics of H-phase in NiTiHf high temperature shape memory alloy



A. Shuitcev^{a,*}, Y. Ren^a, B. Sun^b, G.V. Markova^c, L. Li^a, Y.X. Tong^{a,*}, Y.F. Zheng^{d,*}

- ^a Institute of Materials Processing and Intelligent Manufacturing, College of Materials Science and Chemical Engineering, Harbin Engineering University, Harbin 150001, China
- b Center of Testing and Analysis, College of Materials Science and Chemical Engineering, Harbin Engineering University, Harbin 150001, China
- ^c Physics of Metal and Material Science Department, Tula State University, Tula 300012, Russian Federation
- ^d School of Materials Science and Engineering, Peking University, Beijing 100871, China

ARTICLE INFO

Article history: Received 13 October 2021 Revised 10 November 2021 Accepted 11 November 2021 Available online 13 January 2022

Keywords: High temperature shape memory alloys NiTiHf

Time-temperature-transformation diagram Coarsening kinetics H-phase

ABSTRACT

Precipitate hardening is the most easiest and effective way to enhance strain recovery properties in NiTiHf high-temperature shape memory alloys. This paper discusses the precipitation, coarsening and age hardening of H-phase precipitates in $Ni_{50}Ti_{30}Hf_{20}$ alloy during isothermal aging at temperatures between 450 °C and 650 °C for time to 75 h. The H-phase mean size and volume fraction were determined using transmission electron microscopy. Precipitation kinetics was analyzed using the Johnson-Mehl-Avrami-Kolmogorov equation and an Arrhenius type law. From these analyses, a Time-Temperature-Transformation diagram was constructed. The evolution of H-phase size suggests classical matrix diffusion limited Lifshitz-Slyozov-Wagner coarsening for all considered temperatures. The coarsening rate constants of H-phase precipitation have been determined using a modified coarsening rate equation for non-dilute solutions. Critical size of H-phase precipitates for breaking down the precipitate/matrix interface coherency was estimated through a combination of age hardening and precipitate size evolution data. Moreover, time-temperature-hardness diagram was constructed from the precipitation and coarsening kinetics and age hardening of H-phase precipitates in $Ni_{50}Ti_{30}Hf_{20}$ alloy.

© 2022 Published by Elsevier Ltd on behalf of The editorial office of Journal of Materials Science & Technology.

1. Introduction

High-temperature shape memory alloys (HTSMAs) have attracted much attention due to their potential applications in automotive, aerospace, nuclear and other engineering fields [1,2]. Among all the reported HTSMAs, NiTiHf alloys have been regarded as one of the most promising candidates for practical applications in the temperature range up to 300 °C due to their controllable martensitic transformation (MT) temperature, shape recovery properties and lower cost compared with NiTiX (X=Pt, Pd, Au) alloys [1–4]. Most of the functional properties of shape memory alloys (SMAs) are related to the reversible thermoelastic MT.

Now the aged NiTiHf alloys have demonstrated good thermal cycle stability [5–7], perfect superelastic behavior [5,8,9], high work output [10,11] and good one- [5,8,12] and two-way [13] shape memory through precipitation hardening. For example, stable two-way shape memory behavior with actuation strain

E-mail addresses: alex.tsu2008@yandex.ru (A. Shuitcev), tongyx@hrbeu.edu.cn (Y.X. Tong), yfzheng@pku.edu.cn (Y.F. Zheng).

of 3.2% was achieved in the aged $Ni_{50.3}Ti_{29.7}Hf_{20}$ alloy even after 1600–2000 cycles [7,13]. Moreover, high-temperature superelasticity with fully recovered strain of 4% in tension and compression was achieved in aged $Ni_{50.3}Ti_{29.7}Hf_{20}$ alloy due to the formation of nano-scale (~20 nm) precipitates [5,9].

Precipitation hardening remains one of the most effective ways in the development of ultrahigh-strength alloys. In Ni-Ti-Hf system, nano-scale precipitates of H-phase (or H-precipitate) can be formed in B2 matrix in alloys with Ni contents slightly exceeding 50 at.% during aging [3,4]. However, H-phase was initially found and identified (orthorhombic, space group $(F_{\frac{2}{d}}^{\frac{2}{d}} \frac{2}{d})$) in aged Ni_{48.5}Ti_{36.5}Hf₁₅ alloy by Han et al. [14]. Later, Yang et al. [15] confirmed that and proposed an atomic structure model for H-phase by ab initio calculations, which contains 192 atoms in the conventional unit cell. MT temperatures are very sensitive to precipitation [12,16,17]. Short duration low-temperature aging leads to the formation of dense distribution of small precipitates with limited interparticle spacing, which in turn made martensite nucleation more difficult and decreased transformation temperatures (TTs). After longer-duration aging at low-temperature or elevatedtemperature aging, the volume fraction of precipitate increases as

^{*} Corresponding authors.

well as depletion of Ni in the alloy matrix, which results in an increase in TT with aging time [12]. Precipitation leads to a change in the chemical composition of the matrix. For example, the composition of the matrix for $\rm Ni_{50.3}Ti_{29.7}Hf_{20}$ alloy aged at 600 °C for 815 h determined by atom probe tomography method was estimated to be 49.8 at.% of Ni, 31.2 at.% of Ti and 19.0 at.% of Hf [15]. Recently, Yu et al. [18] investigated H-phase precipitation in NiTiHf alloy and its effect on MT by phase field simulation method and found that the concentration fields of Ni and Hf and inhomogeneous stress around an H-phase precipitate are responsible for the changes in TTs at short and long aging durations, respectively.

Despite the fact that a large number of works have been devoted to precipitation hardening in NiTiHf alloys, the clear quantitative relationships between the H-phase parameters (size and volume fraction) and strength level are still lacking. It should be noted that the quantification of precipitation hardening is a challenging subject as it demands the combined knowledge of precipitation strengthening mechanism and growth and coarsening kinetics. Santamarta et al. [19] gave a scattered estimate of H-phase particle sizes after different heat treatments for different compositions of NiTiHf alloys. It was also concluded that increasing Ni content of the alloy causes a faster growth of the precipitate and for a fixed Ni content, coarsening of the precipitate is faster when Hf content is increased [19]. Recently, Prasher et al. [20] studied the growth and coarsening kinetics of H-phase in Ni_{50.3}Ti_{29.7}Hf_{20.} alloy by small-angle neutron scattering method and reported that Ni diffusion governs the growth of the H-phase, while the coarsening process is controlled by Hf diffusion. The activation energies for the growth and coarsening were estimated to be 196 and 233 kJ mol^{-1} , respectively [20].

Classical one-peak precipitate hardening behavior was reported for $Ni_{50.3}Ti_{34.7}Hf_{15}$ and $Ni_{50.3}Ti_{29.7}Hf_{20}$ alloys [16,17]. Such behavior was reasonablly explained within the precipitate cutting and the Orowan mechanisms [16,17]. The peak of strength corresponds to the transition from the cutting to the Orowan mechanism. Unfortunately, the correlation between H-phase precipitate parameters in NiTiHf alloys and strengthening mechanisms is still unknown.

In order to fulfill the above-mentioned gap, the present study focuses on the quantification of H-phase parameters on precipitation hardening behavior and MT temperatures in a Ni₅₀Ti₃₀Hf₂₀ (at.%) alloy subjected to isothermal aging at a temperature range between 450 and 650 °C. This composition was not chosen by chance. Such composition guarantees the preservation of high MT temperatures during various heat treatments. To determine the evolution of H-precipitate size, volume fraction and morphology with aging, TEM investigations were performed. Precipitation hardening behavior was estimated by microhardness measurements. The precipitation kinetics was analyzed using the Johnson-Mehl-Avrami-Kolmogorov (JMAK) equation. Coarsening rate constant values were calculated as a function of temperature utilizing the modified Lifshitz-Slyozov-Wagner (LSW) based coarsening model. The activation energy for precipitation and coarsening was calculated. The range of critical sizes in which the hardening mechanisms change each other was determined as a function of temperature. Finally, based on the precipitation and coarsening kinetics and precipitate hardening behavior, time-temperature-hardness (TTH) diagram was calculated for the present alloy to map the effect of aging time and temperature on the resulting strength.

2. Experimental methods

The alloy with a nominal composition of $Ni_{50}Ti_{30}Hf_{20}$ (at.%) was prepared by arc-melting using high purity titanium, nickel and hafnium in a water-cooled copper crucible under an argon atmosphere. Before the melting of the ingot, a pure Ti button was melted and used as an oxygen-getter. The ingot was re-melted

eight times, being flipped over after each melting step to ensure homogeneity in composition. After melting, the ingot was sealed in a quartz tube under vacuum and homogenized at 900 °C for 6 h and solution-treated by water-quenching.

The samples with a thickness of approximately 1 mm were prepared by electro-spark cutting method from the solution-treated ingot. The surface of samples was grinded to remove cutting marks. In order to investigate the precipitation and coarsening kinetics of the H-phase, samples were aged at temperatures between 450 and 650 °C with a duration from 0.1 to 75 h. Aging longer than 1 h was carried out in the evacuated quartz tubes to avoid oxidation. Shorter aging was performed in pre-heated Al_2O_3 crucibles to ensure that the specimens reached the target temperature quickly. After aging, the samples were water-quenched.

The transformation temperatures of the solution-treated and aged samples were measured using a Perkin Elmer diamond differential scanning calorimeter with a heating and cooling rate of 20 °C/min under a nitrogen atmosphere. Each sample was thermally cycled between 80 and 320 °C.

Transmission electron microscopy (TEM) observations were conducted using a Talos 200FX G2 electron microscope operated at 200 kV with a double-tilt stage. The foils for TEM observation were prepared by mechanical grinding to a thickness of 50 μ m, followed by low-temperature ion-milling.

Samples for microhardness testing were first mechanically polished till mirror surface and after that subjected to measurement in an HVS-1000 Vickers microhardness tester. In order to avoid the indentation size effect [21], the load on the indenter was chosen to be 200 g with a loading time of 10 s. At least 20 points were measured and the average value was taken as the microhardness.

The ImageJ software was used to determine the size parameters (length and width) of H-phase precipitates directly from bright-field TEM images. Near 150 precipitates were measured to determine the mean size. The H-precipitate volume fraction was measured using the line-intercept method applied to STEM-HAADF micrographs [22]. The volume fraction reported in this paper is the mean values of twenty independent measurements in randomly chosen areas of each investigated sample. Statistical processing of all the results was carried out using Statgraphics Centurion XV software.

3. Results and discussion

3.1. Age hardening behavior

The evolution of microhardness as a function of aging time for Ni $_{50}$ Ti $_{30}$ Hf $_{20}$ alloy aged at 450, 550, and 650 °C is shown in Fig. 1. The lowest microhardness value of 3.69 \pm 0.06 GPa was recorded for the solution-treated sample. A similar hardness value was previously reported for the alloys with similar compositions [16,23]. In general, a continuous increase of microhardness occurs until the peak value is achieved during aging. The peaks of microhardness at 4.40 \pm 0.10, 4.92 \pm 0.03 and 4.94 \pm 0.03 GPa after aging for 0.5 h at 650 °C, 10 h at 550 °C and 50 h at 450 °C, respectively, are clearly seen. Further aging resulted in a continuous decrease in microhardness. The results are similar with the hardening behavior of Ni-rich composition for NiTiHf and NiTiZr alloys aged at 550 °C [6,16,24], except the peak value of microhardness appear at different aging time due to the difference in Ni content.

It is commonly accepted that a typical one-peak precipitate hardening behavior consists of two stages: before and after the peak of hardness. On the first stage, the resistance of a precipitate against dislocation cutting results in a microhardness increase. On the second stage, a dislocation is forced to loop around the precipitate rather than cutting through. As a rule, the precipitates on the first stage are coherent with the matrix of alloy while on the sec-

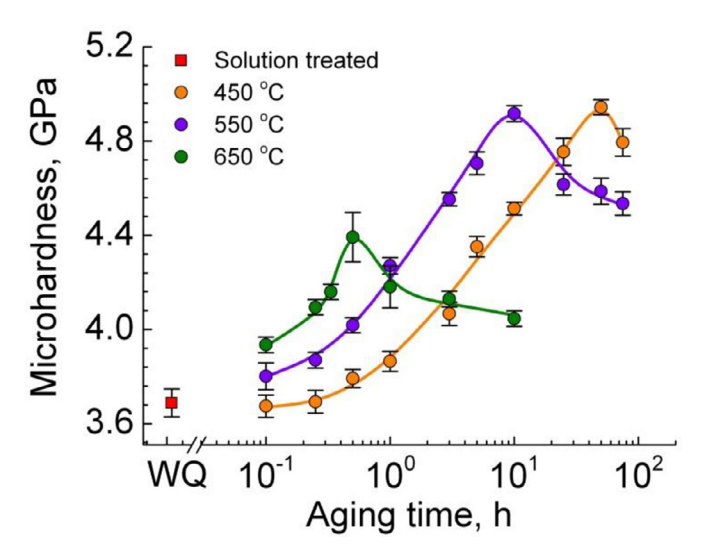


Fig. 1. Evolution of microhardness as a function of aging time for the $Ni_{50}Ti_{30}Hf_{20}$ alloy aged at 450, 550, and 650 °C.

ond stage the coherence is broken down; the boundaries between particle and matrix are incoherent.

3.2. Microstructure characterization of precipitates during aging

No precipitates were observed in the solution-treated samples (Fig. S1 in the Supplementary Information). In this paper, we mainly focused on the evolution of the H-phase precipitate with aging at different temperatures for Ni₅₀Ti₃₀Hf₂₀ alloy. The evolution of martensite phase structure during precipitate aging can be found in Ref [19]. A series of TEM images of the aged Ni₅₀Ti₃₀Hf₂₀ alloy is shown in Fig. 2. Even short-term aging of 6 min at 650 °C is sufficient for precipitation, which agrees well with the microhardness (Fig. 1). The microhardness value increased by \sim 0.25 GPa compared with the solution-treated state. The long and short axes of spindle-shaped precipitates are clearly distinguishable. Two types of structural manifestation of these precipitates can be found. The first type is the uniformly distributed particles into martensitic matrix shown in Fig. 2(a). The second type is mainly a sequential accumulation of particles in the form of "chains" inside the martensitic variants along the inner twins (Fig. 2(b)). Such an arrangement of particles may indicate a significant role of structural defects in their nucleation, in particular, twin dislocations. The precipitates were estimated to have a size with a length of 16.1 \pm 0.7 nm and a width of 7.4 \pm 0.4 nm.

An increase in the duration of aging up to 30 min leads, first of all, to an increase in the precipitate size up to 42.2 ± 2.2 nm and 20.3 ± 1.1 nm for length and width, respectively (Fig. 2(c)). Nevertheless, the regions with a uniform distribution and with a "chain" sequence of particles were preserved, although the length of the "chains" decreased (Fig. 2(c)). A further increase in the aging duration up to 1 h leads to an almost completely homogeneous distribution of particles in the volume of the material as shown in Fig. 2(e).

Homogenous and "chain" distribution of precipitate can also be found at lower aging temperature of 450 °C for 3 h as shown in Fig. 2(f) and (g), respectively. However, the length of "chains" is much smaller than that at higher aging temperatures. By aging at 450 °C for 10 h, the precipitate distribution in martensitic matrix becomes totally homogeneous (Fig. 2(j)). Additionally, it should be mentioned that decreasing aging temperature leads to a significant decrease in the precipitate size and their growth rate. For example,

after aging at 450 °C for 3 and 10 h, the size of precipitates is 3.4 ± 0.1 nm and 3.8 ± 0.1 nm in length and 6.2 ± 0.3 nm and 9.0 ± 0.4 nm in width (Fig. 2(i) and (l)), respectively.

The SAED pattern of the sample aged at 450 °C for 10 h is shown in Fig. 2(k). The pattern taken along the [100] zone axes of B19′ phase with a common plane of (011) type I twins can be clearly identified. Additional reflections corresponding to the H-phase can be found. Fundamental patterns and ¼{210} satellites marked with green triangles and arrows, respectively, are shown on the inset in Fig. 2(k). Similar diffraction patterns were previously reported for Ni-rich NiTiZr and NiTiHf based alloys with H-phase precipitates into B19′ martensitic matrix [19,25].

3.3. Precipitation kinetics of the H-phase

Fig. 3(a–c) shows STEM-HAADF images of Ni $_{50}$ Ti $_{30}$ Hf $_{20}$ alloy after various aging treatments. It is seen that precipitates enriched in Ni and/or Hf due to their brighter contrast than the matrix in STEM-HAADF mode, which is suitable for volume fraction determination. For example, the volume fraction of 4.25% \pm 0.40%, 7.80% \pm 1.65% and 15.97% \pm 1.01% was calculated for the samples aged at 650 °C for 15 min, at 550 °C for 3 h and at 650 °C for 50 h, respectively. The volume fraction was determined by the line-intercept method [22] in 20 randomly chosen areas.

The change in surface area fraction of the H-phase in $Ni_{50}Ti_{30}Hf_{20}$ alloy with aging time and temperature is shown in Fig. 3(d). It is found that aging at the selected temperatures leads to an increase in the H-phase surface area fraction in the alloy matrix to a certain steady-state value, e.g. $16.2\%\pm1.1\%$ at 450 °C, $12.1\%\pm0.9\%$ at 550 °C and $6.1\%\pm0.5\%$ at 650 °C. The shape of the curves resembles a sigmoidal function. Fig. 3(e) shows the measured surface area fractions of the H-phase as a function of temperature after reaching thermodynamic equilibrium at 450, 550 and 650 °C. The equilibrium fraction of the H-phase decreases as the aging temperature increases. Extrapolation of experimental data allows us to estimate the critical temperature above which the H-phase will not be formed. Thus, the solvus temperature for the studied alloy is estimated to be ~ 730 °C.

It is well known that the Johnson-Mehl-Avrami-Kolmogorov (JMAK) equation is most often used to describe the isothermal precipitation kinetics of transformation upon nucleation and growth [26]:

$$f_{t} = f_{\text{equil}}[1 - \exp(-kt^{n})] \tag{1}$$

where f_t is the surface area fraction of the H-phase after aging time t, f_{equil} is surface area fraction after reaching thermodynamic equilibrium state, k is a rate constant and n is the index that describes the nucleation mechanisms [26].

In order to determine n and k values, $\ln(\ln(1/(1-f)))$ is plotted against $\ln(t)$ in Fig. 4(a) for temperatures of 450 to 650 °C. The slope of the resulting lines is the Avrami exponent n, while k can be calculated from the intercept. Plot lines were fitted using the least squared method. It is seen that the experimental data can be well described by a straight line with a high correlation coefficient of R^2 . This means that the JMAK theory can be applied to describe the kinetics of H-phase precipitation in NiTiHf alloy.

The evolution of n parameter as a function of temperature is shown in Fig. 4(b). It is seen that in the studied temperature range, the n parameter decreases from 0.769 ± 0.075 to 0.505 ± 0.029 with an increase in the aging temperature from 450 to 650 °C. The slight change in the n parameter indicates that the mechanism of H-phase nucleation in the matrix of Ni₅₀Ti₃₀Hf₂₀ alloy does not significantly change in the temperature range 450–650 °C. Low values of n near $\frac{7}{3}$ means that the precipitates of H-phase are generated on dislocations [26], which is in good agreement with the results of microstructure (Fig. 2).

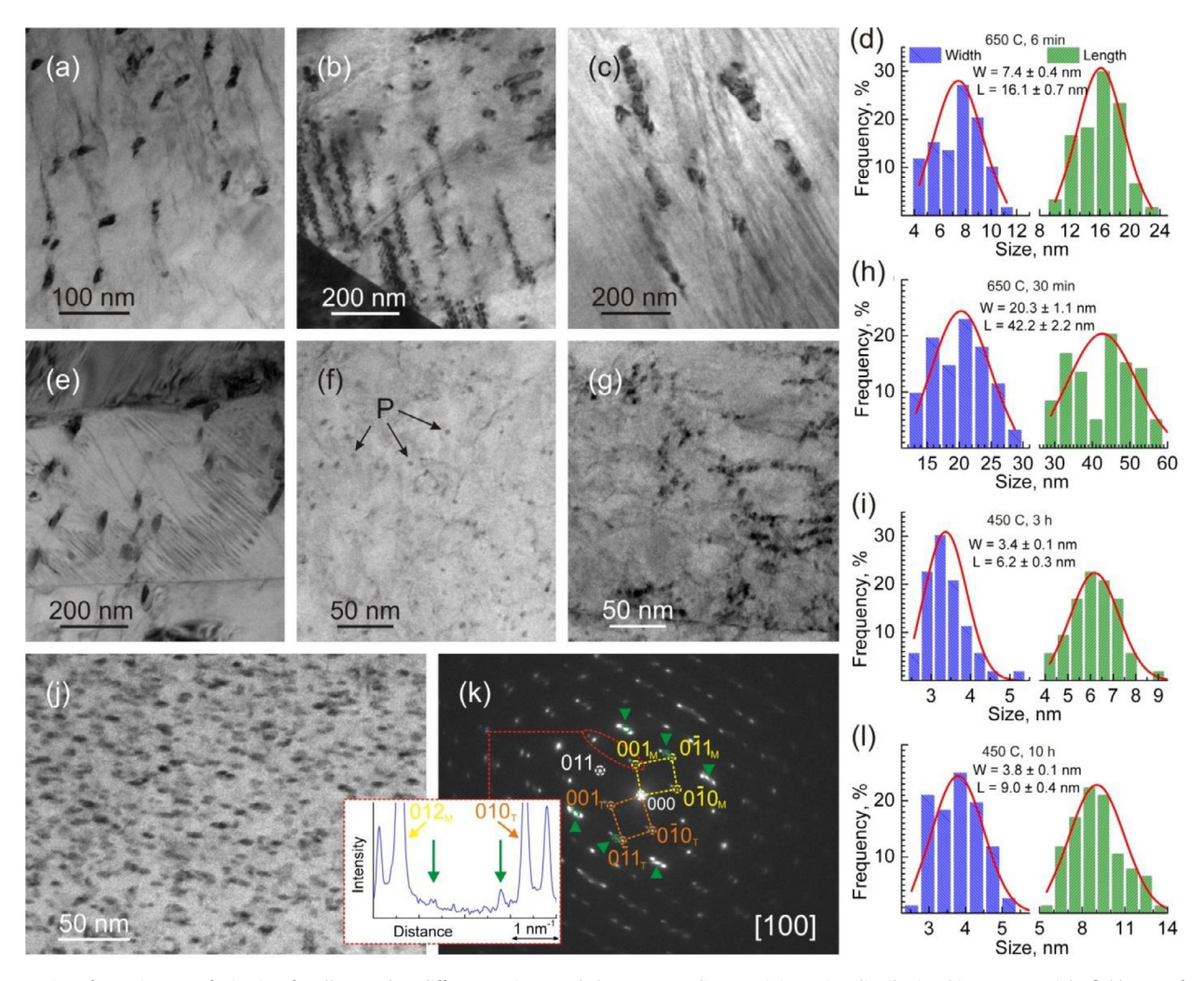


Fig. 2. A series of TEM images of $Ni_{50}Ti_{30}Hf_{20}$ alloy aged at different regimes and the corresponding precipitate size distribution histograms. Bright-field TEM of samples aged at 650 °C for 6 min (a, b), 30 min (c) and 1 h (e). Bright-field TEM of samples aged at 450 °C for 3 h (f, g) and 10 h (j). SAED pattern taken from 10 h aged sample at 450 °C with reflects of H-phase (k). (d, h, i, l) The corresponding precipitate size distribution histograms.

Assuming that the precipitation of the H-phase is a thermally activated process, which can be described by an Arrhenius type of equation, the temperature dependence of k can be written as:

$$k = k_0 \exp\left(-\frac{Q}{RT}\right) \tag{2}$$

where k_0 is rate constant, R is the universal gas constant (8.31 J mol⁻¹ K⁻¹), T is the absolute temperature (in Kelvin) and Q is the apparent activation energy for precipitation. Activation energy can be estimated from the slope of Arrhenius plot in ln(k) versus 1000/T coordinates shown in Fig. 5. For the present alloy, this value is calculated to be 98 ± 12 kJ mol⁻¹. Prasher et al. [20] previously estimated the activation energy for H-phase growth in $Ni_{50.3}Ti_{29.7}Hf_{20}$ alloy to be 196 kJ mol⁻¹ and proposed that Ni-diffusion governed the H-precipitate growth. This looks quite doubtful since the difference in the concentrations of Ni in the alloy matrix and in the particle of H-phase is not large [15,16].

The calculated activation energy for precipitation is significantly lower compared to the diffusion activation energy for Ni (143 kJ mol⁻¹) and Ti (205 kJ mol⁻¹) in B2 phase of NiTi alloy [27]. It is well known that the diffusion in B2 compounds occurs mainly by the vacancy mechanism, which allows not to violate the long range order of a system [28]. Baturin and Lotkov [29], using positrons annihilation method, determined the energy of vacancy formation on

the Ti sublattice in $Ni_{50}Ti_{50}$ alloy as equal to 94 kJ mol⁻¹. Later, Kulkova et al. [30] theoretically calculated that the formation of antisite defects is also energetically beneficial in NiTi alloys. The formation energy of titanium antisite defect in the nickel sublattice was calculated to be 93 kJ mol⁻¹ [31]. Santamarta et al. [19] noted that H-phase precipitates faster as the Ni content of alloy increases. The shift away from the stoichiometric composition towards an increase in the Ni content in NiTiHf matrix should lead to an increase in the density of point defects on the Ti/Hf sublattice. This is caused by the need to preserve the long-range order in B2 phase. It can be assumed that the formation of the H-phase occurs as follows. Vacancies on the titanium sublattice are dominated in the solution-treated state in the studied alloy because of the Ni composition (slightly more than 50 at.%). During aging, Ni atoms occupy positions in Ti sublattice because it is energetically beneficial [30] and does not require large energy costs. The formation energy of Ni antisite defect in Ti sublattice is $44 \text{ kJ} \text{ mol}^{-1}$ [31]. In this case, the formation of Ti antisite defects on Ni sublattice will be a limiting process leading to the formation of H-phase.

Any way, it is obvious that defects play a key role in the nucleation of H-phase in NiTiHf alloy. The small value of the activation energy and "chain" sequence of H-particle along the inner twins of martensitic variants on the earlier stages of precipitation (Fig. 2(b) and (g)) supports such assumption.

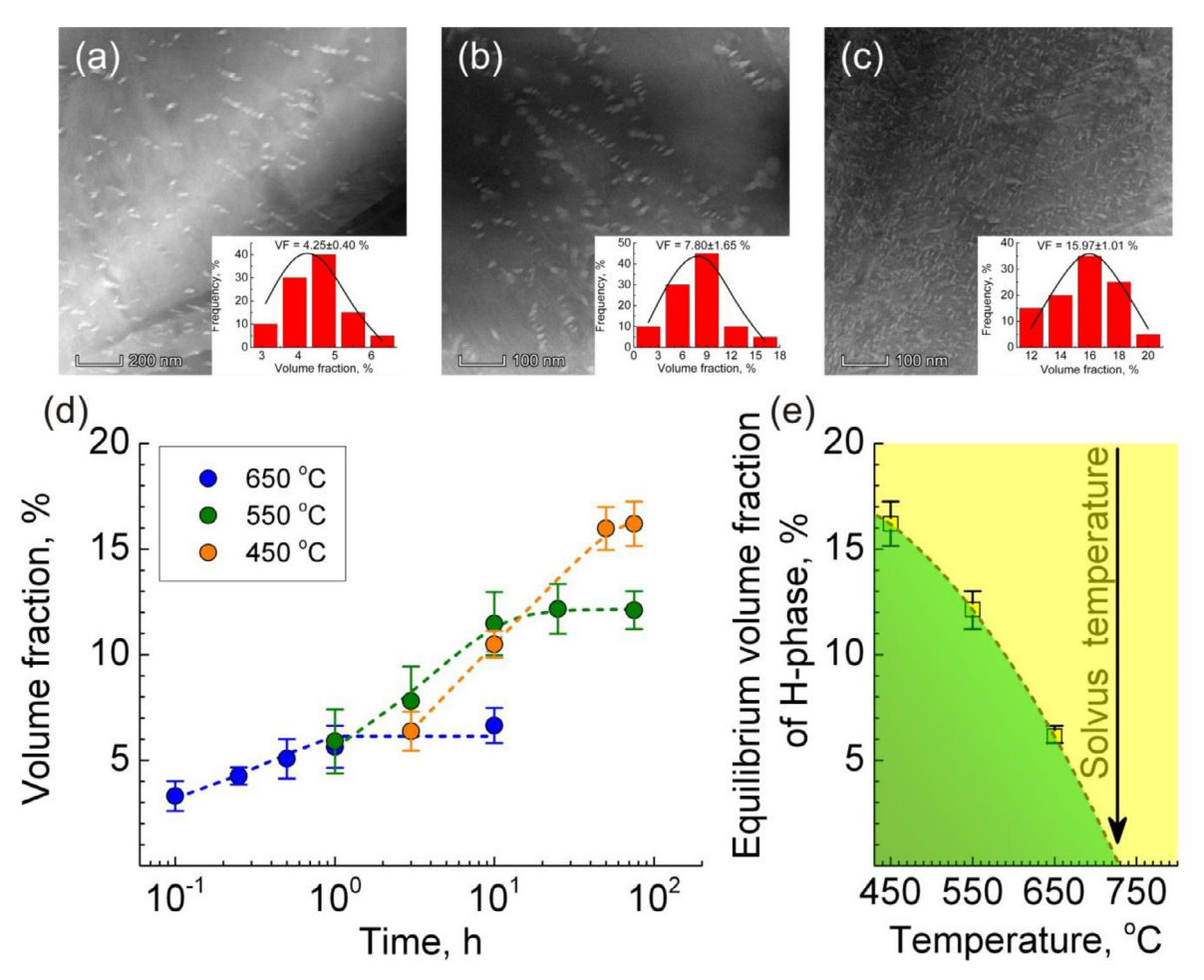


Fig. 3. Typical STEM-HAADF images of $Ni_{50}Ti_{30}Hf_{20}$ alloy aged at 650 °C for 15 min (a), 550 °C for 3 h (b) and 450 °C for 50 h (c). The insets in (a–c) show the volume fraction distribution histograms. Evolution of surface area fraction of the H-phase in the polycrystalline matrix of $Ni_{50}Ti_{30}Hf_{20}$ alloy for the aging temperatures ranging from 450 °C to 650 °C (d) and the temperature dependence of the volume fraction of the H-phase at thermodynamic equilibrium state (e). Note: in figure volume fraction presented in% while all calculations were carried out in relative parts.

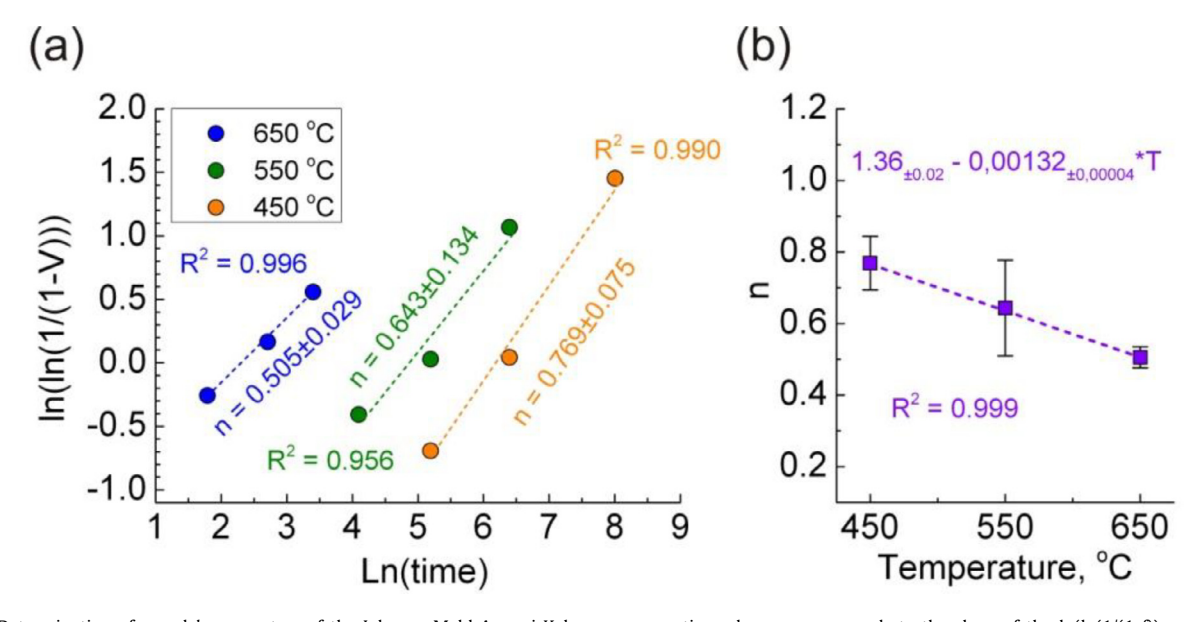


Fig. 4. (a) Determination of n and k parameters of the Johnson-Mehl-Avrami-Kolmogorov equation where n corresponds to the slope of the $\ln(\ln(1/(1-f)))$ versus $\ln(t)$ plot while k can be calculated from the intercept. (b) Evolution of n parameter as a function of temperature.

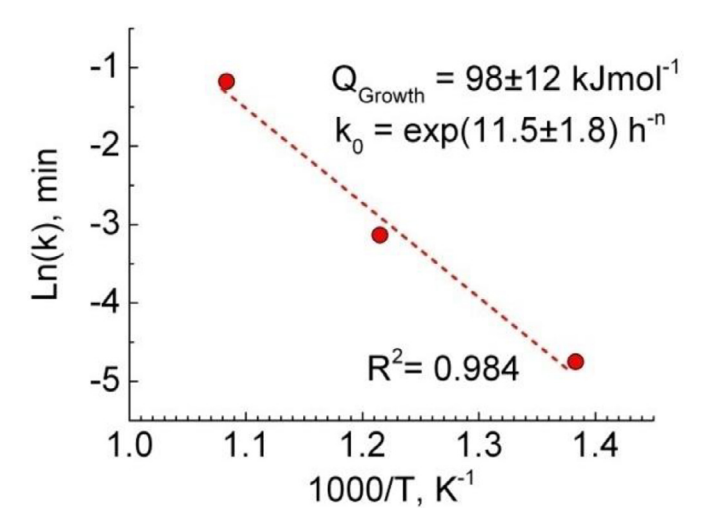


Fig. 5. Arrhenius plots of ln(k) vs. 1000/T for the precipitation kinetics of H-phase in $Ni_{50}Ti_{30}Hf_{20}$ alloy.

3.4. Time-temperature-transformation (TTT) diagram

The TTT diagram was constructed for H-phase formation in Ni-TiHf alloy by combining Eqs. (1) and (2) to obtain the following relationship:

$$t = \left\lceil \frac{\ln(100 - f)}{-k_0 \exp\left(-\frac{Q}{RT}\right)} \right\rceil^{\frac{1}{n}}$$
 (3)

The results are plotted in Fig. 6(a). As conventionally defined, the beginning of transformation corresponds to f=1% of transformed fractions, while 50% and 99% correspond to the middle and the end of the transformation, respectively. In the studied temperature range, the H-phase precipitation kinetics are strongly temperature dependent and faster at high temperatures. At 650 °C, precipitation begins in \sim 0.1 s while at 450 °C a longer time (\sim 1.5 min) is required. The precipitation kinetics of the H-phase between solvus temperature and 650 °C were not investigated.

In order to obtain more practically useful results, Eq. (3) and data from Fig. 3(e) were combined to compute a TTT diagram for the volume fraction of H-phase, as shown in Fig. 6(b). Such a TTT diagram can be used to determine the shortest time required to form a given volume fraction of H-phase. For example, volume fractions of 5% and 15% can be formed within \sim 35 min and \sim 31.5 h at 650 °C and 450 °C, respectively.

3.5. Coarsening kinetics of the H-phase

As above-mentioned, the shape of H-phase precipitate in $Ni_{50}Ti_{30}Hf_{20}$ alloy shows a spindle-like shape. The evolution of average length (long axis) and width (short axis) of precipitate during aging at 450, 550 and 650 °C is shown in Fig. 7(a). Several important observations can be drawn from the analysis of data shown in the figure. First of all, aging temperature significantly affects the particle size: the higher the aging temperature, the larger the particle size. For example, during aging for 10 h, the average length of H-phase particles reaches \sim 160, \sim 30 and \sim 9 nm at 650, 550 and 450 °C, respectively. Secondly, the H-phase particles grow much more intensively in length than in width, which is probably due to a decrease in the elastic strain energy of the system.

Table 1Calculated temporal exponent and LSW rate constant.

Temperature, °C	Temporal exponent, n^{-1}	Rate constant K_r , m ³ s ⁻¹
450 550 650	$\begin{array}{c} 0.281 \pm 0.004 \\ 0.297 \pm 0.052 \\ 0.295 \pm 0.031 \end{array}$	4.7•10 ⁻³¹ 2.1•10 ⁻²⁹ 1.294•10 ⁻²⁷

Usually, a precipitate coarsening for dilute systems is described in the framework of the classical Lifshitz-Slyozov-Wagner (LSW) model [32,33]. The LSW model is based on the evaporation of solute atoms from the shrinking particles and its condensation on the growing particles. The exponent of coarsening roughly determines the coarsening mechanism. In the case of LSW model, it is expected to be 3. Since the LSW model considers spherical particles, all calculations will be carried out for the radius equivalent size r. In order to determine the operative mechanism of coarsening of H-phase precipitates in $Ni_{50}Ti_{30}Hf_{20}$ alloy, a plot of ln(r)vs. ln(t) for the studied aging temperatures is shown in Fig. 7(b). The slope of the curves gives the inverse of the temporal exponent values of 0.295 \pm 0.031 at 650 °C, 0.297 \pm 0.052 at 550 °C and 0.281 \pm 0.004 at 450 °C (Table 1). These values are close to the predicted value of 0.33 by the LSW model. It means that the coarsening process is limited by solute diffusion through NiTiHf matrix. It should be noted that at early stage, growth and coarsening processes occur simultaneously. In order to eliminate the effect of growing process, all calculations for coarsening kinetics are carried out after H-phase reached equilibrium volume fraction.

In the case of matrix diffusion-limited coarsening, the temporal evolution of average precipitate size can be expressed as follow:

$$r^3 - r_0^3 = K_{\Gamma} \cdot t \tag{4}$$

where r is the mean radius equivalent size of precipitate at time t, r_0 is the mean radius equivalent size at the aging time, t=0 and $K_{\rm r}$ is coarsening rate constant. The mean radius equivalent size of precipitate for different aging durations at the selected temperatures have been plotted on a graph of $r^3 - r_0^3$ vs. aging time (t) as shown in Fig. 7(b). The calculated coarsening rate constant values (K) are 0.00047 nm³/s at 450 °C, 0.021 nm³/s at 550 °C and 1.294 nm³/s at 650 °C. Thus with an increase in aging temperature of 100 °C, the coarsening rate appears to increase nearly 50 times. The temporal exponent and coarsening rate constant values of precipitate size evolution are summarized in Table 1.

For the diffusion-controlled coarsening processes, the slowest diffusing elements in NiTiHf alloy will limit the coarsening rate. The modified LSW model based coarsening rate constant value (K) can be given as [34]:

$$K_{\rm r} = \frac{8}{9} \frac{\Gamma C_{\rm e} V_{\rm m}^2 D}{RT} \tag{5}$$

where Γ is the interfacial free energy of the particle-matrix interface, D is the diffusion coefficient of the solute atoms in the matrix. $C_{\rm e}$ is the concentration of solute atoms in equilibrium with a particle of infinite radius, R is the Boltzmann constant, T is the aging temperature, $V_{\rm m}$ is the molar volume of the precipitate, and q is the ratio between width and length of precipitate. The diffusion coefficient D can be expressed as:

$$D = D_0 \exp\left(\frac{-Q_{\text{Coars}}}{RT}\right) \tag{6}$$

where D_0 is the pre-exponential factor and Q_{Coars} is the activation energy for the diffusion or in our case for coarsening of precipitates in the alloy. Substituting the expression of D from Eqs. (6) into (5) gives the following relationship:

$$K_{\rm r} = \frac{8}{9} \frac{\Gamma C_{\rm e} V_{\rm m}^2 D_0}{RT} \exp\left(\frac{-Q_{\rm Coars}}{RT}\right) \tag{7}$$

 $^{^1}$ In this case, we are talking about the relative volume fractions with respect to the thermodynamic equilibrium fraction of the H-phase at a given temperature $\it T$, i.e. 0.01, 0.5 and 0.99 of $\it f_{\rm equil}$.

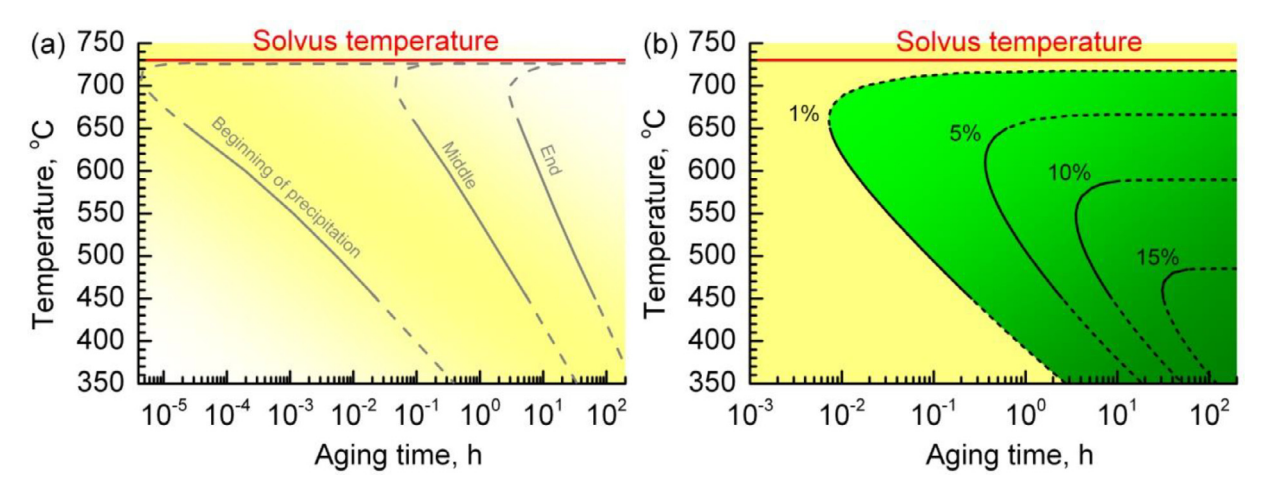


Fig. 6. TTT diagrams of NiTiHf alloy where the red line represents the solvus temperature of the H-phase. (a) TTT diagram where the gray lines mark the beginning, middle and end of H-phase precipitation. (b) TTT diagram showing the volume fractions of H-phase at different time and temperatures. Solid lines represent JMAK model within the considered temperature range and dash lines represent the extrapolated data.

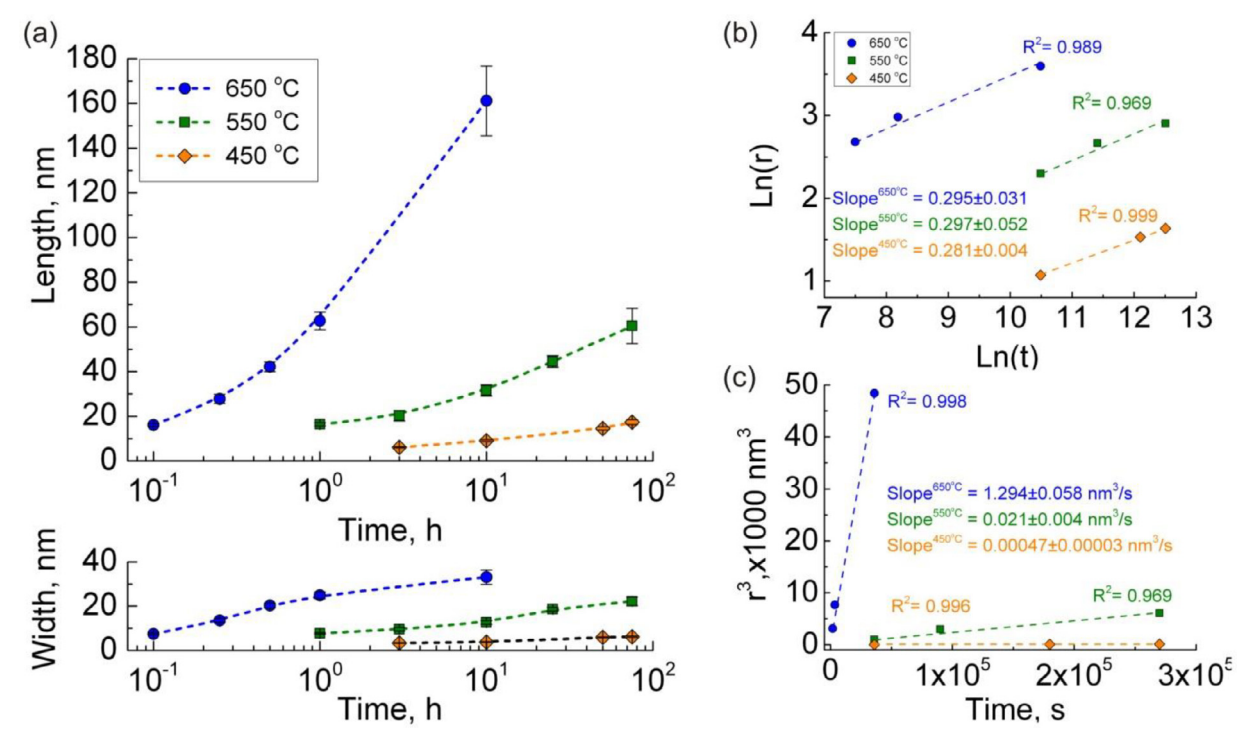


Fig. 7. (a) Temporal evolution of average length and width of H-precipitate of NiTiHf alloy during isothermal aging at 450, 550 and 650 °C. (b) Plots of $\ln(r)$ vs. $\ln(t)$ for isothermal aging temperatures giving temporal growth exponent of H-precipitates, which corresponds to classical LSW growth exponent. (c) Plots showing linear fit of radius equivalent size of H-phase precipitate (r^3 in nm^3) vs. aging time (t) during isothermal aging at 450, 550 and 650 °C along with respective LSW rate constant. .

The expression for the determination of activation energy can be rewritten as follows:

$$\ln\left[\frac{K_{\rm r}T}{\Gamma C_{\rm e}V_{\rm m}^2D_0}\right] = {\rm constant} - \frac{Q_{\rm Coars}}{RT} \tag{8}$$

The slope of the plot between $ln(K_rT)$ vs 1000/T, as shown in Fig. 8, gives the activation energy value of 225 ± 22 kJ mol^{-1} . It is quite difficult to answer unequivocally by the diffusion of which element the coarsening of the H-phase precipitates in the studied alloy is limited, since currently there is no work on diffusion in triple NiTiHf alloys. However, some comparisons can still be made based on the available diffusion data for binary NiTi alloy. Although in this case caution should be exercised because the high content of Hf atoms can affect the diffusion parameters. For example, in

Ref. [35], using the low-frequency internal friction method was analytically determined that the diffusion activation enthalpy of Ni atoms in B2 phase is 137 kJ mol^{-1} and 176 kJ mol^{-1} for $\text{Ni}_{50.6}\text{Ti}_{49.4}$ and $\text{Ni}_{50.3}\text{Ti}_{29.7}\text{Zr}_{20}$ alloys, respectively.

Given that the H-phase is enriched in Hf and depleted in Ti compared to the matrix, diffusion of these elements may control the growth of the H-phase. Low activation energy of Ni diffusion in B2 phase of NiTi alloy also supports such assumption. The activation enthalpy for Ti diffusion in B2 phase of Ni_{50.6}Ti_{49.4} alloy was estimated to be 205 kJ mol⁻¹ [27]. Moreover, the activation energy of self-diffusion in β -Ti is 251.2 kJ mol⁻¹ [36]. From another hand, the same value of activation energy (251.2 kJ mol⁻¹) was found for Hf diffusion in Ti between 550 and 750 °C as well as that for Hf diffusion in Ni in the temperature range of 750–1150 °C [36].

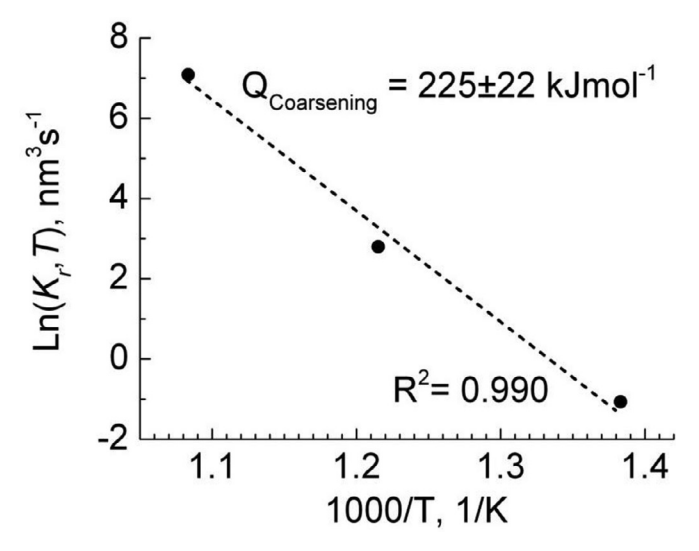


Fig. 8. Plot between the coarsening rate constant $(\ln(K_T, T)$ vs. inverse of heat-treatment temperature (1000/T) with linear fit using linear regression analysis to calculate activation energy $(Q_{\text{Coarsening}})$.

Recently, Prasher et al. [20] estimated the activation energy for the coarsening of H-phase in $\mathrm{Ni}_{50.3}\mathrm{Ti}_{29.7}\mathrm{Hf}_{20}$ alloy as 233 kJ mol^{-1} . They believe that Hf diffusion remained the rate-controlling step for coarsening process. Several reasons also support such an assumption. First of all, Ni diffusion in NiTiHf based alloys can be excluded due to the lower activation energy compared to that for Ti. Secondly, the atom size of Hf $(r_{\mathrm{Hf}} \sim 0.159 \ \mathrm{nm})$ [37] is bigger than Ti $(r_{\mathrm{Ti}} \sim 0.147 \ \mathrm{nm})$ atoms, and hence atoms of Hf can slow diffusion as well. Finally, Santamarta et al. [19] noted that coarsening rate of H-phase increases with increasing Hf content in NiTiHf alloys. For the above-mentioned reasons, it is reasonable to assume that Hf diffusion is a limiting factor in the coarsening of H-phase particles for NiTiHf alloys.

3.6. Breaking down the coherency between H-phase/matrix interface

It is well known that the formation of the H-phase leads to an increase in the strength properties of Ni-rich NiTiHf alloys. As shown in Fig. 1, during continuous aging, the strength first increases and then begins to decrease. It is generally accepted that this behavior is due to a change in the interaction mechanism of dislocations with precipitates. The increase in strength is associated with an increase in the volume fraction of closely spaced precipitates which are cut by moving dislocations (Friedel effect [38]). Overaging leads to coarsening of particles and an increase in interparticle space, which allows dislocations to bend around them and as a result the strength decreases (Orowan mechanism [39]). Nevertheless, it should be noted that even in the case of overaging, the strength of the alloy is higher than that in the solution-treated state. The Orowan mechanism assumes that the precipitate/matrix interface is incoherent. Thus, the transition from one mechanism to another is due to the achievement by the particles of some critical size, at which coherence is disturbed.

The combination of experimental data (Figs. 1 and 7) allows us to establish the H-phase size at which the changes in the precipitation hardening mechanisms occur in $Ni_{50}Ti_{30}Hf_{20}$ alloy. In this case, as a criterion for size, we propose to use the length of the H-phase, because it is the length that increases more intensively with aging. The critical size is chosen at a peak of microhardness upon age hardening. The evolution of the H-phase critical size as a function of aging temperature in $Ni_{50}Ti_{30}Hf_{20}$ alloy is shown in

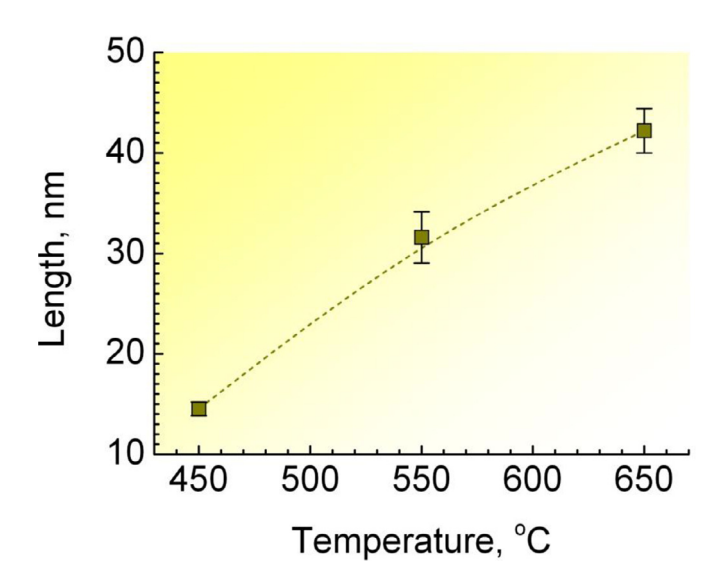


Fig. 9. Evolution of critical size of H-phase precipitates as a function of temperature.

Fig. 9. It is clearly seen that the critical size increases from \sim 15 nm at 450 °C to \sim 42 nm at 650 °C.

In order to shed more light on the evolution of the H-phase critical size during changing the precipitation hardening mechanisms with temperature. HRTEM observation was carried out. Fig. 10(a) and (c) shows HRTEM images of H-precipitate and martensitic matrix in NiTiHf alloy after aging at 650 °C for 30 min and 1 h, respectively. The enlarged HRTEM images of the interface between the H-precipitate and martensitic matrix in the sample aged at 650 °C for 30 min are shown in Fig. 10(b). Good continuity of the atomic planes across the interface can be clearly distinguished, together with a small tilt of these planes at the interface. Lines parallel to these atomic planes show the tilt angle. However, there are also areas (marked by ellipses) with large distortion of the atomic planes. The tilt of atomic planes across the precipitate/matrix interface was also observed by Santamarta et al. [19] in the furnace cooled Ni₅₂Ti₂₈Hf₂₀ alloy. They proposed that the precipitates conserve their original orientation during the MT but the surrounding matrix experiences the shear strain accompanying the transformation, causing the atomic plane tilt. Yu et al. [18] determined that elastic stress-strain fields appear around coherent H-phase precipitate in B2 phase of Ni_{50.3}Ti_{29.7}Hf₂₀ alloy by phase field simulation. It also should be kept in mind that $B2\rightarrow B19'$ MT in NiTiHf alloys accompanied with increases in volume, which can serve as an additional source of stresses [40]. It is obvious that in the example considered on Fig. 10(a) and (b), the martensitic shear leads not only to a small tilt in the atomic planes, but also to their partial distortion. Probably, the distortion of atomic planes allows accommodating the stresses caused by volume changes upon MT. However, the presence of even partial coherency does not lead to a decrease in strength in the studied alloy, which is in good agreement with microhardness data.

An increase in the duration of aging up to 1 h at 650 °C leads to a violation of the continuity of the atomic planes across the precipitate/matrix interface, as shown in Fig. 10(d). Moreover, a small transition layer can be clearly distinguished at the interface between the H-phase and the matrix. In shown case precipitate/matrix interface looks more like semi-coherent than totally incoherent, which is confirmed with the decreasing of microhardness to 4.18 \pm 0.08 GPa. Apparently, there are several ways to disrupt the coherency between the precipitate and the matrix in the studied alloy. In the first case, the coherence breakdown occurs dur-

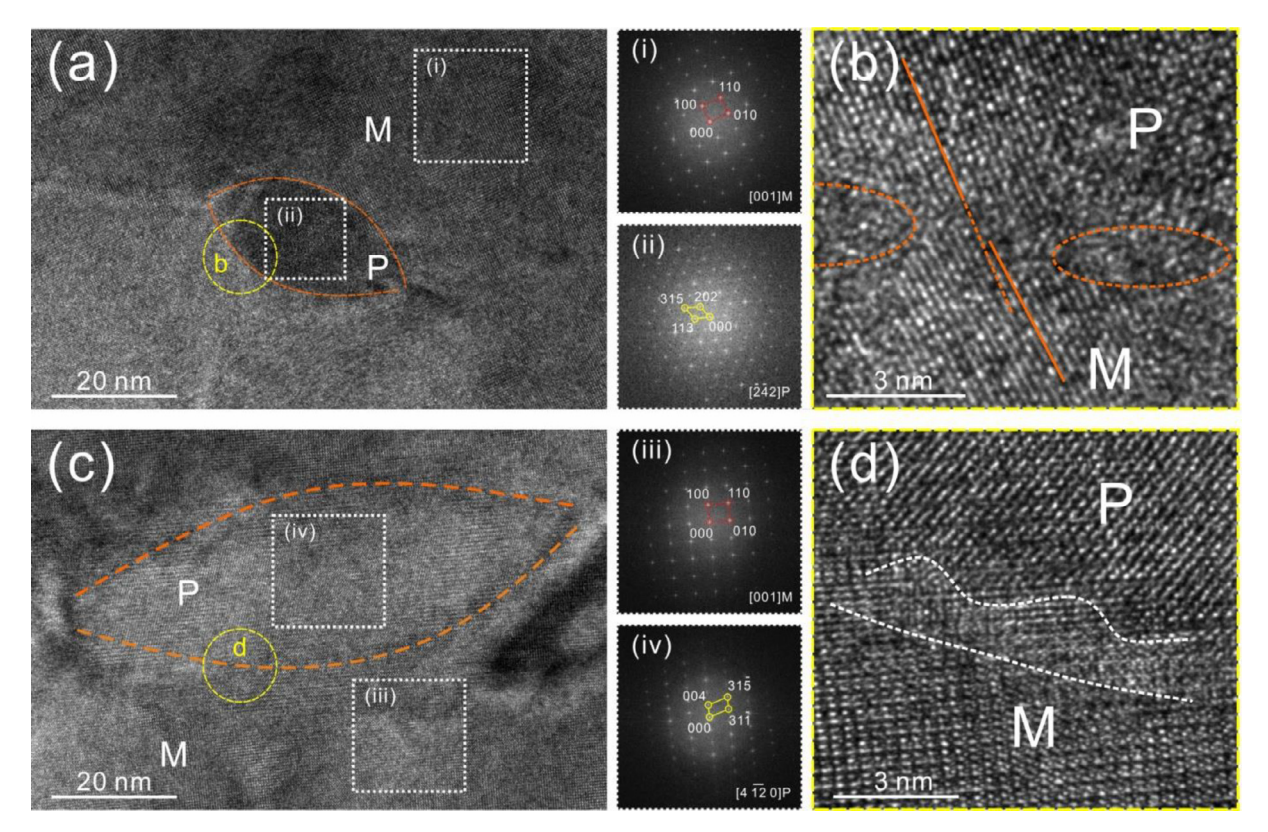


Fig. 10. HRTEM images and corresponding FFT patterns of NiTiHf alloy after 30 min (a, b) and 1 h (c, d) at 650 °C.

ing aging in the austenitic region. The precipitate reaches a critical size, which leads to the appearance of large elastic stresses at the precipitate/matrix interface. Relaxation of these stresses results in a breakdown of coherency. In the second case, the loss of coherence can be caused by a martensitic shear strain, which leads to the tilt of martensitic variants relative to the originally oriented (coherent with the B2 phase) precipitate of H-phase.

A possible reason for the increase in the critical size of H-phase particles upon changing the mechanisms of precipitation hardening with an increase in aging temperature is the abnormal behavior of elastic constants of B2 phase in a wide range of temperatures. This anomaly lies in the fact that in the temperature range of MT, the modulus of elasticity drops sharply and increases with increasing temperature in the austenitic state. Such an anomaly is caused by pre-transition phenomena that facilitate lattice invariant shear upon MT. For example, the elastic modulus of the B2 phase in Ni₅₁Ti₄₉ alloy increases to a temperature of \sim 530 °C [41]. An increase in the elastic modulus indicates an increase in interatomic bonds, which probably provides elastic accommodation of the stress fields surrounding the particles of H-phase. The increase of elastic modulus with temperature is beneficial for maintaining coherence between precipitate/matrix interfaces during precipitate coarsening even at high temperatures. Abnormal behavior of elastic constants of B2 phase was also found in NiTiHf-based alloys [42,43].

3.7. Time-temperature-hardness (TTH) diagram

Conventional precipitation curves are not always convenient for achieving the maximum strength of the alloy by optimizing aging treatment. For NiTiHf HTSMA, it is especially important since the strength is correlated with strain recovery properties [3,5]. Thus, Shercliff and Ashby [44,45] proposed to use TTH diagram, where

the axes are aging temperature and time while the contours are lines of constant hardness (or yield strength).

Fig. 1 shows that Ni₅₀Ti₃₀Hf₂₀ alloy exhibits classical one-peak precipitation hardening behavior. The fine coherent precipitates of H-phase in the alloy impede dislocation movement by forcing dislocations to either cut through the precipitates or go around them. For the cutting mechanism, the contribution of shearable precipitates to the strength of the alloy can be represented by [44]:

$$\Delta HV_{\rm cut} = C_{\rm cut} f_{\rm t}^{0.5} r^{0.5} \tag{9}$$

where ΔHV_{cut} is gain in hardness (defined as difference between hardness in solution-treated and aged states) due to cutting mechanism and C_{cut} is a constant. In order to determine C_{cut} , ΔHV is plotted against $f_t^{0.5}r^{0.5}$ in Fig. 11(a) for temperatures from 450 to 650 °C. Experimental data were fitted using least squares method from which the slope C_{cut} was obtained for different temperatures. The insert in Fig. 11(a) shows the C_{cut} coefficient as a function of temperature. The C_{cut} coefficient decreases from \sim 0.076 to \sim 0.042 with an increasing aging temperature from 450 to 650 °C.

As the precipitate grows, the coherence between the precipitate and matrix is broken down and dislocation can no longer cut precipitates. In this case, bypassing mechanism can be rewritten in a form [44]:

$$\Delta HV_{\rm b} = C_{\rm b} \frac{f_{\rm t}^{0.5}}{r} \tag{10}$$

where ΔHV_b is gain in hardness due to bypassing mechanism and C_b is a constant. Correlation between $f_t^{0.5}/r$ and ΔHV_b is shown in Fig. 11(b). The C_b coefficient increases from \sim 5 to \sim 15 with an increasing aging temperature from 450 to 650 °C (inset in Fig. 11(b)).

Precipitate cutting and bypassing are alternative processes. The contribution of precipitation to the strength from the cutting and bypassing precipitates can be defined as:

$$\Delta HV = \begin{cases} C_{\rm cut} f_{\rm t}^{0.5} r^{0.5}, & r \le r_{\rm cr} \sim L_{\rm cr} \\ C_{\rm b} \frac{f_{\rm t}^{0.5}}{r}, & r > r_{\rm cr} \sim L_{\rm cr} \end{cases}$$
 (11)

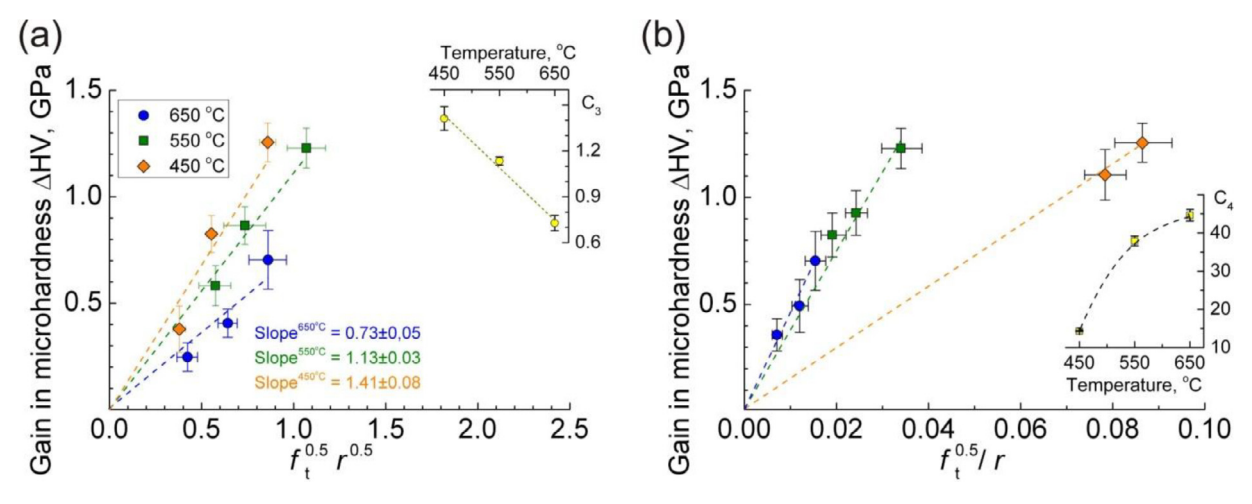


Fig. 11. The gain in hardness (Δ HV) as a function of $f_t^{0.5}L^{0.5}$ (a) and $f_t^{0.5}/L$ (b). The insets in (a) and (b) show the temperature dependence of $C_{\rm cut}$ and $C_{\rm b}$ constants, respectively.

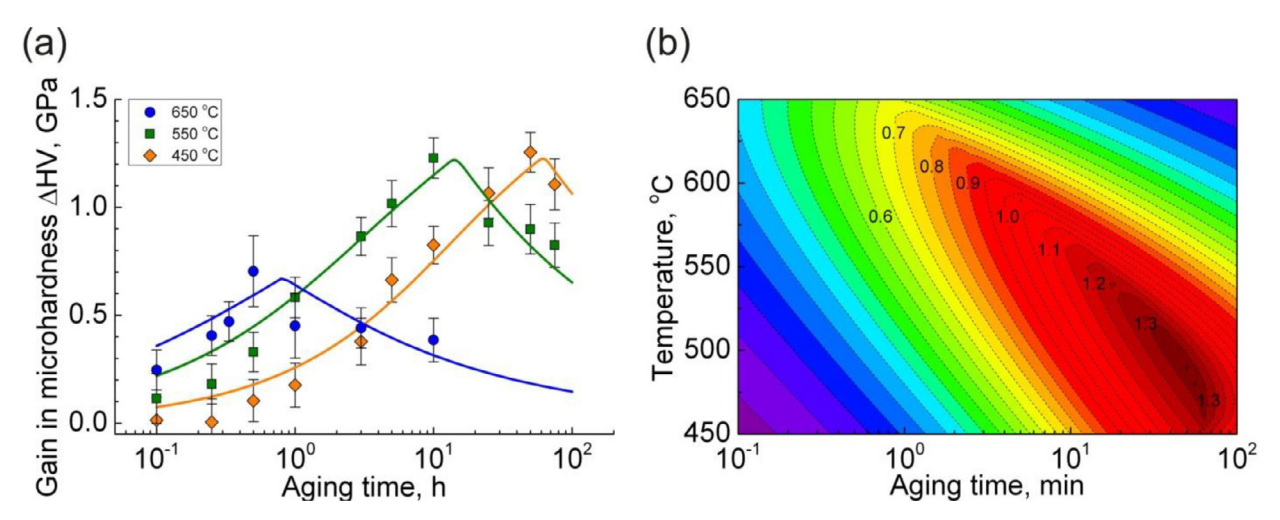


Fig. 12. (a) Data from the present study for $Ni_{50}Ti_{30}Hf_{20}$ alloy compared with the model of Eq. (11). (b) TTH diagrams of aged $Ni_{50}Ti_{30}Hf_{20}$ alloy.

The volume fraction (f_t) and size (equivalent r) parameters can be taken from Sections 3.3 and 3.5, respectively. In this calculation, as a critical size ($r_{\rm cr}$), we propose to use the lower limit of the range of H-phase sizes at which changes in the precipitate hardening mechanisms occur in Ni₅₀Ti₃₀Hf₂₀ alloy (defined in Section 3.6, Fig. 12).

Fig. 12(a) shows the calculated gain in hardness (Δ HV) in comparison with experimental data for Ni₅₀Ti₃₀Hf₂₀ alloy aged at various temperatures. The agreement between calculated and experimental data is good enough. Using the same approach, TTH diagram of the studied alloy is plotted in Fig. 12(b) as a function of aging treatment. The peak of hardness on the TTH diagram is a ridge which rises as the temperature falls and the duration of aging increases. Obviously, such behavior of the ridge of strength is due to an increase in the equilibrium volume fraction of H-phase in the matrix of Ni₅₀Ti₃₀Hf₂₀alloy.

3.8. Influence of H-phase precipitates on transformation temperature

MT peak temperatures (M_p) were determined from the DSC curves shown in Fig. S2 and were summarized in Fig. 13(a). At the aging temperatures of 550 and 650 °C, M_p temperature continuously increased. Transformation temperature corresponding to aging at 550 °C increases more intensively than that at 650 °C. At a lower aging temperature of 450 °C, M_p deceased from \sim 195 °C for

the solution-treated state to \sim 185 °C for 1 h aging. After that transformation temperatures continuously increased with increasing aging time. A similar dependence of transformation temperatures on aging time was previously reported for the aged Ni_{50.3}Ti_{34.7}Hf₁₅ [12] and Ni_{50.3}Ti_{29.7}Hf₂₀ [5] alloys.

The continuous increase in MT temperature at high-temperature aging or long-duration aging at lower temperatures is due to the dominance of the so-called "chemical" (or "compositional") effect caused by the formation of the H-phase [12,18]. It is commonly accepted that the essence of the effect is the depletion of Ni in the Ni-rich B2 matrix. Yu et al. [18] confirmed by phase fields simulation that the concentration of Ni and Hf in B2 matrix of Ni_{50.3}Ti_{29.7}Hf₂₀ alloy around the precipitate is inhomogeneous and keeps changing during aging until reaches the equilibrium state. The decrease in MT temperature during low-temperature aging is due to the dominance of the "mechanical" effect associated with H-phase precipitation. The essence of the effect is the presence of a high volume fraction of nanoscale precipitates, with very limited interparticle spacing, which creates elastic stress fields that prevent the development of martensitic shear strain [12].

In present work, the "mechanical" effect does not affect the M_p of the samples aged at 550 and 650 °C. This is possibly due to the "mechanical" effect being very short in time because precipitate size grows very fast, which is in good agreement with the

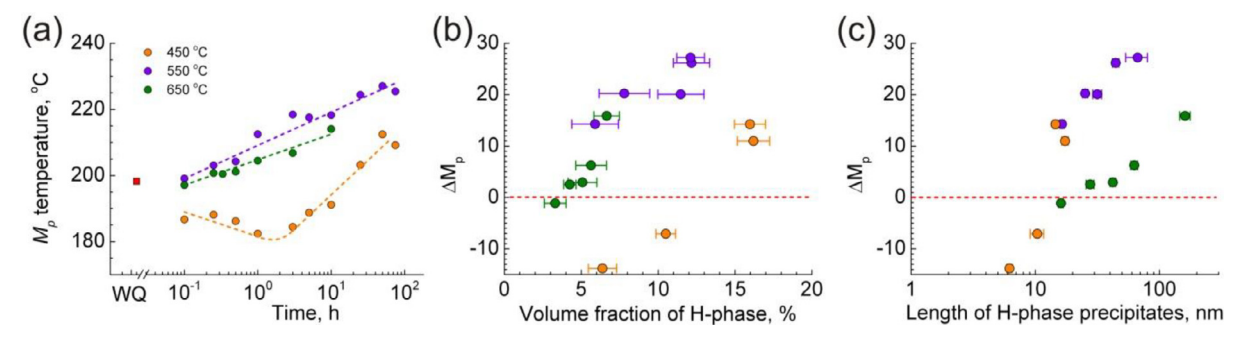


Fig. 13. Evolution of M_p temperatures as a function of aging time for $Ni_{50}Ti_{30}Hf_{20}$ alloy (a) and the influence of volume fraction (b) and size (c) of H-phase on ΔM_p temperature.

experimental result on the coarsening rate of H-phase precipitates described in the previous Section 3.5. The role of volume fraction and size of H-phase on $M_{\rm p}$ temperature and the corresponding effects can be drawn for the samples aged at 450 °C. Fig. 13(b) and (c) shows the effect of the volume fraction and the size of H-phase on $\Delta M_{\rm p}$ (difference between the solution-treated and aged samples), respectively. When aging at 450 °C, the transition from "mechanical" to "chemical" effect of H-phase particles influence on $M_{\rm p}$ temperature occurs when the particle reaches a size of \sim 6 nm (in length of precipitate) and volume fraction of \sim 6%. Nevertheless, the "chemical" effect dominates even at a small volume fraction of \sim 3% for the case of 650 °C aging. Apparently, the precipitate size is the determining factor in the competition between these two effects.

4. Conclusions

- (1) Aging at a temperature range of 450–650 °C leads to the H-phase precipitation in Ni₅₀Ti₃₀Hf₂₀ alloy. Two different microstructures are identified at all aging temperatures: one is the homogeneously distributed H-phase precipitates; and another one is the chain-like H-phase precipitates distributed mostly along the inner twins. The latter disappears with increasing aging duration.
- (2) $Ni_{50}Ti_{30}Hf_{20}$ alloy shows the classical one-peak precipitation hardening behavior. The H-phase solvus temperature is determined to be ~ 730 °C by extrapolating the equilibrium volume fraction.
- (3) The precipitation of the H-phase during aging follows the Johnson-Mehl-Avrami-Kolmogorov equation. The temperature dependence of the precipitation kinetics can be well described by an Arrhenius type of law with an activation energy of 98 ± 12 kJ mol $^{-1}$, which is in good agreement with the literature value for the formation energy of Ti antisite defects on Ni sublattice. Such a small value indicates the significant role of vacancies in precipitation.
- (4) A TTT diagram for H-phase precipitation was constructed for $Ni_{50}Ti_{30}Hf_{20}$ alloy aged at temperatures between 450 and 650 °C.
- (5) The temporal exponents of average H-phase size for $Ni_{50}Ti_{30}Hf_{20}$ alloy aged at 450, 550 and 650 °C are close to the values predicted by Lifshitz-Slyozov-Wagner model, suggesting matrix diffusion is the coarsening rate limiting step. The activation energy for H-precipitates coarsening is estimated to be 225 \pm 25 kJ mol $^{-1}$. The coarsening of H-phase is controlled by the Hf diffusion in NiTiHf alloy matrix.
- (6) The critical size of H-phase responsible for breaking down the coherency between matrix and precipitate is determined. The critical size increases with increasing aging temperature, presumably due to anomalies of the elastic con-

- stants behavior of the B2 matrix caused by pre-transition phenomena.
- (7) By combining the precipitation and coarsening kinetics with the age hardening behavior of H-phase precipitates, TTH diagram for $Ni_{50}Ti_{30}Hf_{20}$ alloy is constructed for a temperature range of 450–650 °C and duration up to 100 h.

Supporting information

xyz

Acknowledgments

This study is financially supported by the National Natural Science Foundation of China (Nos. 52050410340 and 51971072), and the Fundamental Research Funds for the Central University (No. 3072021CF]1002).

Supplementary materials

Supplementary material associated with this article can be found, in the online version, at doi:10.1016/j.imst.2021.11.011.

References

- [1] J. Ma, I. Karaman, R.D. Noebe, Int. Mater. Rev. 55 (2010) 257–315.
- [2] J. Van Humbeeck, Mater. Res. Bull. 47 (2012) 2966–2968.
- [3] H.E. Karaca, E. Acar, H. Tobe, S.M. Saghaian, Mater. Sci. Technol. 30 (2014) 1530–1544.
- [4] Y.X. Tong, A.V. Shuitcev, Y.F. Zheng, Adv. Eng. Mater. 22 (2020) 1900496.
- [5] H.E. Karaca, S.M. Saghaian, G. Ded, H. Tobe, B. Basaran, H.J. Maier, R.D. Noebe, Y.I. Chumlyakov, Acta Mater. 61 (2013) 7422–7431.
- [6] X.L. Meng, W. Cai, F. Chen, L.C. Zhao, Scr. Mater. 54 (2006) 1599-1604.
- [7] O. Karakoc, K.C. Atli, A. Evirgen, J. Pons, R. Santamarta, O. Benafan, R.D. Noebe, I. Karaman, Mater. Sci. Eng. A 794 (2020) 139857.
- [8] G.S. Bigelow, A. Garg, S.A. Padula II, D.J. Gaydosh, R.D. Noebe, Scr. Mater. 64 (2011) 725–728.
- [9] S.M. Saghaian, H.E. Karaca, M. Souri, A.S. Turabi, R.D. Noebe, Mater. Des. 101 (2016) 340–345.
- [10] H.E. Karaca, E. Acar, G.S. Ded, B. Basaran, H. Tobe, R.D. Noebe, G.S. Bigelow, Y.I. Chumlyakov, Acta Mater. 61 (2013) 5036–5049.
 [11] S.M. Saghaian, H.E. Karaca, H. Tobe, A.S. Turabi, S. Saedi, S.E. Saghaian,
- Y.I. Chumlyakov, R.D. Noebe, Acta Mater. 134 (2017) 211–220. [12] A. Evirgen, I. Karaman, R. Santamarta, J. Pons, R.D. Noebe, Acta Mater. 83
- (2015) 48-60. [13] C. Hayrettin, O. Karakoc, I. Karaman, J.H. Mabe, R. Santamarta, J. Pons, Acta
- Mater. 163 (2019) 1–13. [14] X.D. Han, R. Wang, Z. Zhang, D.Z. Yang, Acta Mater. 46 (1998) 273–281.
- [15] F. Yang, D.R. Coughlin, P.J. Phillips, L. Yang, A. Devaraj, L. Kovarik, R.D. Noebe, M.J. Mills, Acta Mater. 61 (2013) 3335–3346.
- [16] B.C. Hornbuckle, T.T. Sasakì, G.S. Bigelow, R.D. Noebe, M.L. Weaver, G.B. Thompson, Mater. Sci. Eng. A 637 (2015) 63–69.
- [17] M. Moshref-Javadi, S.H. Seyedein, M.T. Salehi, M.R. Aboutalebi, Acta Mater. 61 (2013) 2583–2594.
- [18] T.W. Yu, Y.P. Gao, L. Casalena, P. Anderson, M. Mills, Y.Z. Wang, Acta Mater. 208 (2021) 116651.
- [19] R. Santamarta, R. Arroyave, J. Pons, A. Evirgen, I. Karaman, H.E. Karaca, R.D. Noebe, Acta Mater. 61 (2013) 6191–6206.

- [20] M. Prasher, D. Sen, J. Bahadur, R. Tewari, M. Krishnan, J. Alloy. Compd. 779 (2019) 630-642.
- [21] A.V. Shuitcev, Y.X. Tong, L. Li, Vacuum 160 (2019) 25–30.
 [22] J.C. Russ, R.T. Dehoff, Practical Stereology, 2nd ed., Springer Science+Business Media, New York, 2000.
- [23] A. Shuitcev, D.V. Gunderov, B. Sun, L. Li, R.Z. Valiev, Y.X. Tong, J. Mater. Sci. Technol. 52 (2020) 218–225.
- [24] S.M. Kornegay, M. Kapoor, B.C. Hornbuckle, D. Tweddle, M.L. Weaver, O. Benafan, G.B. Bigelow, R.D. Noebe, G.B. Thompson, Mater. Sci. Eng. A 801 (2021) 140401
- [25] Y.X. Tong, X.M. Fan, A. Shuitcev, F. Chen, B. Tian, L. Li, Y.F. Zheng, J. Alloy. Compd. 845 (2020) 156331.
- [26] J.W. Christian, The Theory of Transformations in Metals and Alloys, Pergamon, Oxford, 2002.
- [27] S.V. Divinski, I. Stloukal, L. Kral, C. Herzig, Defect Diffus. Forum 289-292 (2009) 377-382 Fam Plan West Hemisph.

- [28] Y. Mishin, C. Herzig, Acta Mater. 48 (2000) 589–623.
 [29] A.A. Baturin, A.I. Lotkov, Phys. Met. Metall. 76 (1993) 168–170.
 [30] S.E. Kulkova, A.V. Bakulin, Q.M. Hu, R. Yang, Phys. B 426 (2013) 118–126.
- [31] S.E. Kulkova, A.V. Bakulin, Q.M. Hu, R. Yang, Mater. Today Proc 2S (2015) S615-S618.

- [32] I.M. Lifshitz, V.V. Slyozov, J. Phys. Chem. Solids 19 (1961) 35-50.
- [33] C. Wagner, Z. Elektrochem. 65 (1961) 581-591.
- [34] J.D. Boyd, R.B. Nicholson, Acta Metall. 19 (1971) 1379-1391. [35] S. Zuo, R. Wu, G. Pang, Y. Yang, M. Jin, Intermetallics 109 (2019) 174–178.
- [36] H. Mehrer, in: Diffusion in Solid Metals and Alloys, Springer Berlin Heidelberg, Berlin, 1990, p. 747.
- [37] N.N. Greenwood, A. Earnshaw, Chemistry of the Elements, Elsevier Butterworth-Heinemann, Oxford, 2012.
- [38] J. Friedel, Dislocations, Pergamon Press, London, 1964.
- [39] R.E. Smallman, R.J. Bishop, in: Modern Physical Metallurgy and Materials Engineering, Butterworth-Heinemann, Oxford, 1999, p. 438.
- [40] A. Shuitcev, R.N. Vasin, X.M. Fan, A.M. Balagurov, I.A. Bobrikov, L. Li, I.S. Golovin, Y.X. Tong, Scr. Mater. 178 (2020) 67–70.
- [41] R. Hasiguti, K. Iwasaki, J. Appl. Phys. 39 (1968) 2182–2186.
 [42] M. Perez-Cerrato, B. Maass, M.L. No, J. San Juan, J. Alloy. Compd. 856 (2021) 157948.
- [43] A. Shuitcev, L. Li, G.V. Markova, I.S. Golovin, Y.X. Tong, Mater. Lett. 262 (2020) 127025
- [44] H.R. Shercliff, M.F. Ashby, Acta Metall. Mater. 38 (1990) 1789–1802.
- [45] H.R. Shercliff, M.F. Ashby, Acta Metall. Mater. 38 (1990) 1803–1812.